Neutron scattering study of the $Tm_2Ir_2O_7$ pyrochlore iridate

M. Klicpera,[1,*] K. Vlášková,[1] D. Staško,[1] T. Guidi,[2,3] I. Puente Orench,[4,5] and M. Diviš[1]

[1]*Charles University, Faculty of Mathematics and Physics, Department of Condensed Matter Physics, Ke Karlovu 5, 121 16 Prague 2, Czech Republic*

[2]*ISIS Facility, Rutherford Appleton Laboratory, Chilton, Didcot, Oxon OX11 0QX, United Kingdom*

[3]*Physics Division, School of Science and Technology, University of Camerino, I-62032 Camerino, Italy*

[4]*Institut Laue-Langevin, 71 avenue des Martyrs, CS 20156, 38042 Grenoble Cedex 9, France*

[5]*Instituto de Nanociencia y Materiales de Aragón, CSIC, Pedro Cerbuna 12, 50009 Zaragoza, Spain*

(Received 9 March 2022; revised 12 August 2022; accepted 18 August 2022; published 7 September 2022)

The newly synthesized $Tm_2Ir_2O_7$ iridate is investigated using neutron scattering techniques. Powder neutron diffraction patterns confirm that $Tm_2Ir_2O_7$ crystallizes in a cubic structure of pyrochlore type, consistent with the rest of the rare-earth $A_2Ir_2O_7$ series, and the crystal structure is preserved down to 0.2 K. The thermal expansion of the crystal lattice is well described by a Debye model of lattice vibrations. A weak magnetic signal consistent with the so-called all-in-all-out magnetic order (AIAO) is traced at low temperature; however, it cannot serve as unambiguous evidence of the AIAO structure in the compound. Nondispersive magnetic excitations in energy-momentum space are observed in inelastic neutron scattering spectra of $Tm_2Ir_2O_7$. The crystal-field scheme and parameters of the thulium iridate are refined and discussed with respect to the specific heat and magnetization data. The results are supported by mean-field calculations.

DOI: 10.1103/PhysRevB.106.094408

I. INTRODUCTION

The $A_2T_2O_7$ family of compounds, where A stands for a rare-earth element and T is a transition element, has been studied intensively for its complex structural, magnetic, and conductive properties. The majority of $A_2T_2O_7$ crystallizes in an ordered structure of the pyrochlore type (space group *Fd-3m*, no. 227, origin choice: 2), consisting of individual A and T nets of interpenetrating corner-sharing tetrahedra and oxygen 8- and 6-coordinate cages around the respective cations [1]. The geometrically frustrated lattice significantly affects the magnetic behavior/ground state of the $A_2T_2O_7$ members with A or/and T being magnetic, e.g., the unconventional spin-glass state in $Y_2Mo_2O_7$ [2], the ordered spin ice state in $Tb_2Sn_2O_7$ [3], the spin ice states in $Dy_2Ti_2O_7$ and $Ho_2Ti_2O_7$ [4], the chiral spin-liquid state in $Pr_2Ir_2O_7$ [5], or the structural disorder-induced quantum spin-liquid state in $Pr_2Zr_2O_7$ [6]. Partially ordered systems [7] and fragmentation of magnetic moments in $Dy_2Ir_2O_7$ [8] or $Ho_2Ir_2O_7$ [9] have also been reported. Furthermore, magnetic sublattices A and T can strongly affect each other [10,11]. The *d-f* exchange (T and A spins) [12] could lead to, e.g., anisotropy-tuned magnetic order as in $Er_2Ir_2O_7$ and $Tb_2Ir_2O_7$ [13] or giant magnetoresistance observed in $Nd_2Ir_2O_7$ [14]. The competition and delicate balance among exchange, dipolar, and spin-orbit (SO) interactions in pyrochlores have been proposed and observed to generate topologically nontrivial phases, e.g., a Weyl semimetal state and Fermi-arc surface states (in $Eu_2Ir_2O_7$) [15,16], a topological band insulator, or a topological Mott insulator [17,18].

Focusing on $A_2Ir_2O_7$ iridates, the subject of our present work, they crystallize in the pyrochlore structure. The iridium sublattice orders magnetically below ordering temperature, T_{Ir}, in the majority of members, $Pr_2Ir_2O_7$ being an exception [15,19,20]. The magnetic order of an iridium sublattice has been repeatedly reported to be all-in-all-out (AIAO) order, i.e., neutron diffraction experiments evidenced a magnetic signal consistent with the AIAO order for $Nd_2Ir_2O_7$ [21], $Eu_2Ir_2O_7$ [22], $Dy_2Ir_2O_7$ [8], $Tb_2Ir_2O_7$ [10], $Yb_2Ir_2O_7$, and $Lu_2Ir_2O_7$ [23]. Concomitantly with magnetic ordering, metallic (A = Pr, Nd) or semimetallic/nonmetallic (A = Sm-Lu) $A_2Ir_2O_7$ undergo a transition to the insulating state below T_{Ir} [19]. The rare-earth moments are subject to the Ir molecular field through *d-f* coupling, which might result in induced AIAO magnetic order of the A sublattice—evidenced by neutron diffraction experiment in $Nd_2Ir_2O_7$ [21] and $Tb_2Ir_2O_7$ [10]. Importantly, the second *XY* component of the Tb magnetic moments in $Tb_2Ir_2O_7$ was identified at low temperature, leading to a tilt of the total magnetic moments from the local ⟨111⟩ direction of AIAO order. An antiferromagnetic coupling between Ir and Sm, as well as a long-range ordering of Sm moments, were inferred by analyzing the μSR spectra of $Sm_2Ir_2O_7$ [24]. A ferromagnetic order of Yb moments in $Yb_2Ir_2O_7$ is not fully established down to 40 mK due to phase competition caused by a coupling with the AIAO order of an iridium sublattice [23].

In addition to the long-range Ir order, the induced A order (of magnetic rare-earth ions), and the A-A magnetic correlations, the low-temperature behavior of $A_2Ir_2O_7$ is defined by the A single-ion properties, namely the crystal field (CF)

*Corresponding author: mi.klicpera@seznam.cz

acting on the A cation. The crystal-field schemes of heavy rare-earth $A_2Ir_2O_7$ compounds have been studied systematically by inelastic neutron scattering—$Dy_2Ir_2O_7$ [8], $Ho_2Ir_2O_7$ [9], $Er_2Ir_2O_7$ [25], and $Yb_2Ir_2O_7$ [23]—and confronted with macroscopic data [20,25,26]. Recently, we synthesized and thoroughly characterized the previously unreported $Tm_2Ir_2O_7$ member of the family [20]. Experimental data allowed us to update and complete the $A_2Ir_2O_7$ phase diagram of T_{Ir} [15,19,20], confirm the nonmagnetic Tm ground-state crystal-field singlet, and propose a CF model for $Tm_2Ir_2O_7$. Determination and parametrization of the crystal field in the $Tm_2Ir_2O_7$ iridate acting on Tm^{3+} cations are the subject of the present study. Simultaneously, a neutron diffraction experiment was performed to inspect the magnetic order of the Ir sublattice.

II. SAMPLE SYNTHESIS AND CHARACTERIZATION

Polycrystalline samples of $Tm_2Ir_2O_7$ and $Lu_2Ir_2O_7$ were synthesized from a stoichiometric mixture of A_2O_3 and IrO_2 (AlfaAesar, purity 99.99% metal basis) using the CsCl flux method. The initial oxides were individually heated to 500 K to remove water, weighted in a 1:2 ratio, and thoroughly mixed with CsCl salt (99.999%) in a 1:50 ratio. The mixture was placed in an open Pt crucible and reacted at 1120 K for three weeks with 14 intermediate grindings. The CsCl salt was washed off the samples. Further details on sample preparation have been published elsewhere [27]. The samples were synthesized in large amounts [6.9 and 4.2 g of $Tm_2Ir_2O_7$ for MARI and D1B experiments (see below), and 5.7 g of $Lu_2Ir_2O_7$] to be directly used for the present neutron scattering experiments.

The quality of the samples was checked by x-ray diffraction (Bruker D8-Advance diffractometer with Cu $K\alpha$ radiation) and scanning electron microscopy [MIRA, Tescan, with backscattered-electron (BSE) and energy-dispersive x-ray (EDX) detectors]; see Fig. 1. The x-ray diffraction patterns confirmed the cubic pyrochlore structure (*Fd-3m*) of prepared samples. About 3% of unreacted A_2O_3 oxides was evidenced in the samples of total mass 4.2 and 5.7 g, while the $Tm_2Ir_2O_7$ sample (6.9 g) later used for inelastic neutron scattering experiment contained about 12% of unreacted Tm_2O_3. Unreacted initial oxides in the sample are a common problem preparing $A_2Ir_2O_7$ iridates [5,10,13,25,28] due to significantly different melting temperatures of initial oxides and heavy sublimation of iridium dioxide (in contrast with, e.g., isostructural rare-earth titanates [29] or zirconates [36]). The decomposition and evaporation of IrO_2 are mostly suppressed using the flux, in which the oxides are dissolved, allowing a lower reaction temperature [27]. Nevertheless, synthesizing a large amount of the sample—which is certainly preferable considering the samples' homogeneity and the requirements of neutron scattering techniques for sample volume—is still complicated, and a presence of unreacted oxides cannot be fully suppressed (14 reaction cycles in the present case did not eliminate all Tm_2O_3 in the sample).

The FULLPROF suite [30] was employed to determine the lattice parameter $a^{\mathrm{Tm2Ir2O7}} = 10.135(1)$ Å and $a^{\mathrm{Lu2Ir2O7}} = 10.104(1)$ Å, and the fraction coordinate of the oxygen atom [Wyckoff position $48f$: ($x_{\mathrm{O\text{-}48f}}$, 1/8, 1/8)]

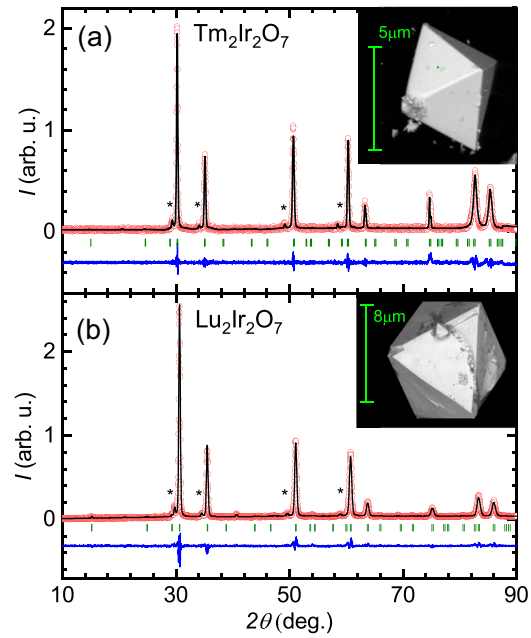

FIG. 1. X-ray diffraction patterns of investigated $Tm_2Ir_2O_7$ and $Lu_2Ir_2O_7$ iridates. The experimental data (red circles), the fit of the data to the pyrochlore model (black line), the difference between the experimental and calculated data (blue line), and the positions of the Bragg reflections of the pyrochlore phase (green ticks) are presented. Peaks of the A_2O_3 phase are marked by asterisks. The insets contain the BSE images of selected single crystalline grains of μm sizes.

$x^{\mathrm{Tm2Ir2O7}}_{\mathrm{O\text{-}48f}} = 0.335(2)$ and $x^{\mathrm{Lu2Ir2O7}}_{\mathrm{O\text{-}48}f} = 0.342(3)$ from diffraction patterns. We note perfect agreement comparing the crystallographic parameters of the previously synthesized sample (a mass of approximately 0.5 g) [20] and the present large amount sample. Furthermore, a pronounced bipyramid shape of synthesized grains (of μm sizes; see the BSE images in the inset of Fig. 1) documents both the good quality of the material and its pyrochlore structure. The stoichiometry ratio A:Ir = 50(2):50(2) was confirmed by the EDX technique; the technique is not sufficiently sensitive to light elements, and therefore the oxygen content cannot be determined.

III. EXPERIMENTAL METHODS AND CALCULATIONS

The neutron diffraction experiment was performed using the D1B diffractometer at the Institute Laue-Langevin (ILL), Grenoble. Monochromatic neutron radiation with a 2.528 Å wavelength, and a multidetector with an angular range of 128 ° and a step of 0.1 ° between each of the 1280 ^{3}He detection cells, were employed (see e.g. [31,32] for details). The $Tm_2Ir_2O_7$ powder sample was loaded in a cylindrical copper container to ensure good thermal contact, of 6 mm diam and 60 mm height mounted on a dilution insert stick. The dilution insert was placed inside a cryofurnace, allowing accurate temperature control from sub-Kelvin temperatures (0.2 K) to 550 K. Parasitic diffraction peaks arising from the cryofurnace were removed by a radial oscillating collimator. The measured diffraction patterns, available in the datasets [33], were processed using the FULLPROF suite [30].

The inelastic neutron scattering (INS) experiments on $A_2Ir_2O_7$ were performed on the time-of-flight spectrometer MARI at the ISIS pulsed neutron and muon source, Rutherford Appleton Laboratory, Didcot, UK. The samples were packed in aluminum foil, in an annular geometry, and placed inside an aluminum cylindrical sample holder with a diameter of 4 cm. The measurements were conducted in a standard closed-cycle refrigerator at temperatures of 5, 100, and 200 K. The incident energies (E_i) were selected by phasing the Gd Fermi chopper in repetition-rate multiplication mode, allowing us to measure two sets of simultaneous energies, namely 10 and 120 meV, and 10, 30, and 180 meV. Auxiliary measurements of an empty container and vanadium for calibration purposes were performed. Data were corrected for container scattering, absorption, and self-shielding, and for detector efficiency variation. The normalization to a vanadium standard allowed the calculation of the dynamic structure factor $S(Q,\omega)$ in absolute units, employing the software package MANTIDPLOT [34]. Normalized spectra were corrected for sample absorption by assuming an evenly loaded sample, similarly to that in the case of other heavy rare-earth analogs [23,25]. The experimental data are accessible in datasets [35].

The magnetization and specific-heat measurements were conducted employing the Magnetic Properties Measurement System and the Physical Properties Measurement System (MPMS and PPMS, Quantum design). Part of the sample was cold-pressed, and a small pellet (≈5 mg) was cut off the pressed sample. Magnetization was measured employing the reciprocating sample option (RSO) at a temperature down to 2 K. The low-temperature magnetization (from 0.4 to 5.0 K) was evaluated indirectly by measuring the electrical resistivity signal of precalibrated Hall probes, Arepoc Company in PPMS [36,37]. Magnetization data were measured in a magnetic field up to 7 T. A standard time-relaxation method and PPMS were used for specific-heat measurements in the temperature interval from 0.4 to 300.0 K.

The model crystal-field (CF) parameters to fit the $Tm_2Ir_2O_7$ inelastic neutron scattering spectra were obtained from the CF parameters of $Er_2Ir_2O_7$ [25] and $Yb_2Ir_2O_7$ [23] by scaling the corresponding Stevens factors. In the case of $Yb_2Ir_2O_7$, the transformation was made from Wybourne to Stevens convention [20]. The respective CF parameters and eigenenergies are listed in Table I. The CF parameters divided by Stevens factors are presented for all heavy rare-earth $A_2Ir_2O_7$ (A = Dy, Ho, Er, Tm, Yb) in Table II for completeness. The final set of CF parameters determined by analyzing the experimental INS data, together with the external magnetic field, was used to construct the microscopic Hamiltonian containing the CF and Zeeman terms. The numerical diagonalization of the microscopic Hamiltonian provided eigenfunctions and eigenenergies. Magnetization as a function of temperature and external magnetic field, and the Schottky contribution to specific heat, were calculated using our in-house computer codes (for details, see [26]).

TABLE I. The crystal-field parameters in Stevens notation and corresponding CF eigenenergies. Model $Tm_2Ir_2O_7$ schemes derived by scaling the CF parameters of $Er_2Ir_2O_7$ [25] and $Yb_2Ir_2O_7$ [23] by Stevens factors (Er→Tm) and transforming the Wybourne CF parameters into Stevens notation (Yb→Tm), and the CF parameters refined from the **INS** spectra of $Tm_2Ir_2O_7$ are listed. Singlet states are marked (s); the other levels are doublets.

	$Tm_2Ir_2O_7^{Er2Ir2O7}$	$Tm_2Ir_2O_7^{Yb2Ir2O7}$	$\mathbf{Tm_2Ir_2O_7^{INS}}$
B_2^0 (10^{-2} meV)	29.670	36.670	**18.277**
B_4^0 (10^{-3} meV)	6.949	5.265	**5.057**
B_4^3 (10^{-2} meV)	4.228	5.602	**3.184**
B_6^0 (10^{-6} meV)	−26.330	−29.470	**−31.260**
B_6^3 (10^{-4} meV)	3.981	7.166	**3.873**
B_6^6 (10^{-4} meV)	−6.554	−4.398	**−5.890**
E_0 (meV)	0 (s)	0 (s)	**0** (s)
E_1 (meV)	8.733	13.733	**10.467**
E_2 (meV)	37.646	24.359 (s)	**33.827** (s)
E_3 (meV)	37.935 (s)	32.418	**36.734**
E_4 (meV)	65.429	60.740	**56.559**
E_5 (meV)	83.915	71.550 (s)	**72.768** (s)
E_6 (meV)	86.147 (s)	75.259	**73.868**
E_7 (meV)	117.112 (s)	110.438 (s)	**89.239** (s)
E_8 (meV)	121.177 (s)	113.829 (s)	**95.250** (s)

IV. NEUTRON DIFFRACTION—LATTICE THERMAL EXPANSION AND SIGNS OF AIAO ORDER

The long-range ordering of the iridium magnetic moments in $Tm_2Ir_2O_7$ was studied by powder neutron diffraction down to 0.2 K. The Tm^{3+} ion in $Tm_2Ir_2O_7$ crystal field reveals a singlet ground state (see Sec. V), therefore no long-range magnetic ordering is expected for a Tm sublattice. That is, only the magnetic signal of an iridium sublattice is investigated by neutron diffraction.

Diffraction patterns recorded in the whole temperature range, above an Ir sublattice magnetic transition [20] as well as below T_{Ir}, are described by the pyrochlore structure. A diffraction pattern measured at 180 K, that is, at a paramagnetic state, is presented in Fig. 2. Bragg reflections corresponding to $Tm_2Ir_2O_7$ pyrochlore structure are marked by green ticks and respective *hkl* indices. Signals arising from a copper sample container (Cu) and from unreacted Tm_2O_3 oxide (*) are labeled. We note that the refined volume fraction of thulium oxide is lower than 1.5%, in good agreement with XRD analysis.

TABLE II. CF parameters divided by Stevens factors for $A_2Ir_2O_7$ pyrochlore iridates. The values are provided in meV units. The initial CF parameters (for A =) were taken from the literature: Dy [8], Ho [9], Er [25], Tm (present study), and Yb [23].

A	Dy	Ho	Er	Tm	Yb
B_2^0/α	32.050	32.000	29.358	18.094	36.300
B_4^0/β	38.375	30.250	42.477	30.977	32.250
B_4^3/β	267.111	210.021	258.558	195.040	343.133
B_6^0/γ	8.088	5.563	4.696	5.576	5.256
B_6^3/γ	−116.175	−106.312	−71.162	−69.086	−127.831
B_6^6/γ	66.019	85.493	116.815	105.065	78.463

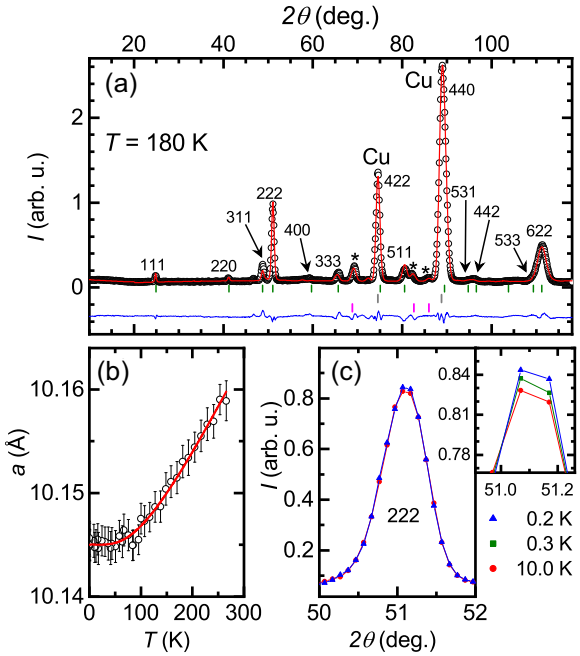

FIG. 2. Neutron diffraction experiment on $Tm_2Ir_2O_7$. (a) Powder neutron diffraction pattern recorded at 180 K: experimental data (black circles), model structure fit (red line), difference between experimental and calculated data (blue line), and positions of Bragg reflections of pyrochlore phase, copper, and Tm_2O_3 (green, gray, and pink ticks) are shown together with reflections marked (Cu for copper and asterisks for Tm_2O_3). (b) Temperature development of the pyrochlore lattice parameter a. The fit to the Debye model of the lattice expansion (1) is plotted as a red line. (c) Temperature development of the 222 peak of pyrochlore structure and zoomed-in detail.

The pyrochlore structure of $Tm_2Ir_2O_7$ is preserved down to 0.2 K; no structural transition is observed. The lattice parameter a decreases approximately linearly down to 80 K and tends to saturate at lower temperature. A thermal expansion of the crystal lattice can be described within a Debye model of lattice vibrations. For a cubic material, the temperature development of the lattice parameter can be described by the following formula:

$$a = a_0[1 + I_0 T\, \phi(\theta_D/T)], \tag{1}$$

where a_0 is the lattice parameter extrapolated to 0 K ($= 10.145$ Å), and I_0 [fitted as $1.02(6) \times 10^{-5}$] is proportional to the product of the isothermal expansion and the Grüneisen parameter [38]. $\phi(\theta_D/T)$ represents a polynomial approximation of the Debye integral. Fitting the data, the Debye temperature θ_D was determined to equal 380(30) K, which is in good agreement with the Debye temperature previously calculated for $Lu_2Ir_2O_7$ analog from the specific-heat data [$\theta_D = 350(4)$ K] [39]. This agreement, *inter alia*, justifies the use of lutetium analog as a good approximation of the contribution of the lattice to $Tm_2Ir_2O_7$ data (see Sec. V).

When searching for a magnetic signal below $T_{Ir}^{Tm2Ir2O7} = 142$ K, no clear evidence of magnetic ordering is observed. No additional peaks outside of the nuclear reflections' positions are tracked out. Focusing on a development of intensity of nuclear peaks, a subtle increase of intensity was followed on 222 reflection [Fig. 2(c)]. We tend to ascribe this signal to the AIAO structure of the Ir moments, similar to that previously reported for other $A_2Ir_2O_7$ (A = Nd [21], Tb [10], Dy [8], Yb, and Lu [23]). However, in contrast to previous studies, no additional magnetic signal—namely, on reflections 220 and 311—was found in the diffraction patterns measured below T_{Ir}. Moreover, the magnetic signal is visible only at low temperature below 10 K, that is, significantly below T_{Ir} (see also Sec. VI). Therefore, based on measured data, the AIAO type of ordering of an Ir sublattice in $Tm_2Ir_2O_7$ cannot be unambiguously acknowledged.

V. INELASTIC NEUTRON SCATTERING—CRYSTAL-FIELD SCHEME OF $Tm_2Ir_2O_7$

The inelastic neutron scattering (INS) spectra of $Tm_2Ir_2O_7$ and $Lu_2Ir_2O_7$ were collected with four incident neutron energies at three temperatures as described above. Lattice excitations (phonons) are observed in INS spectra of both $A_2Ir_2O_7$ members, while additional magnetic excitations, namely crystal-field excitations, are followed in the $Tm_2Ir_2O_7$ spectra. Magnetic excitations related to Ir^{4+} are expected at significantly higher energy [40–42] than those of A^{3+}, and one can suppose that they are similar in Tm and Lu analogs. Simultaneously, almost identical phonon signals in both isostructural analogs are expected. The atomic mass of Tm and Lu, the crystallographic parameters of $Tm_2Ir_2O_7$ and $Lu_2Ir_2O_7$ (see Sec. II), as well as the Debye temperature (Sec. IV and Ref. [39]) are similar. Therefore, the lutetium iridate data can be effectively used to subtract any phonon contribution from the $Tm_2Ir_2O_7$ spectra, and in turn to study magnetic excitations connected with the Tm^{3+} ion. Prior to the subtraction, the data were corrected and normalized (see Sec. III); and considering the different neutron scattering cross sections of the Tm and Lu ions, the $Lu_2Ir_2O_7$ data were multiplied by the ratio between these scattering cross sections ($= 0.9772$). $Tm_2Ir_2O_7$, $Lu_2Ir_2O_7$, and their difference spectra measured with incident neutron energies of 30, 120, and 180 meV at 5 K are presented in Fig. 3. The difference spectra contain, with good accuracy, only magnetic excitations connected with the Tm^{3+} ion in the crystal environment.

Inspecting the difference data, the so-called difference ΔE-Q maps (ΔE stands for energy transfer; $|\mathbf{Q}| \equiv Q$ is the momentum transfer), several nondispersive magnetic excitations are unambiguously identified: excitations at around 4, 8, 10, 35, and 55 meV at 5 K (Fig. 3). No clear additional magnetic excitations are detected at higher energies, up to 150 meV. The magnetic origin of the observed signal is proven by its Q-dependence: The intensity of excitations becomes weaker with increasing Q following the Q-dependence of the magnetic form factor of Tm^{3+}, as well as with increasing temperature (in comparison with the lattice excitations becoming more intense with increasing temperature).

We note that the spectra contain, in addition to magnetic excitations of $Tm_2Ir_2O_7$, also excitations connected with unreacted Tm_2O_3. Thulium oxide crystallizes in cubic structure described by space group *Ia-3* (no. 206) with Tm occupying two nonequivalent positions: 8*b* and 24*d* [43]. Point group

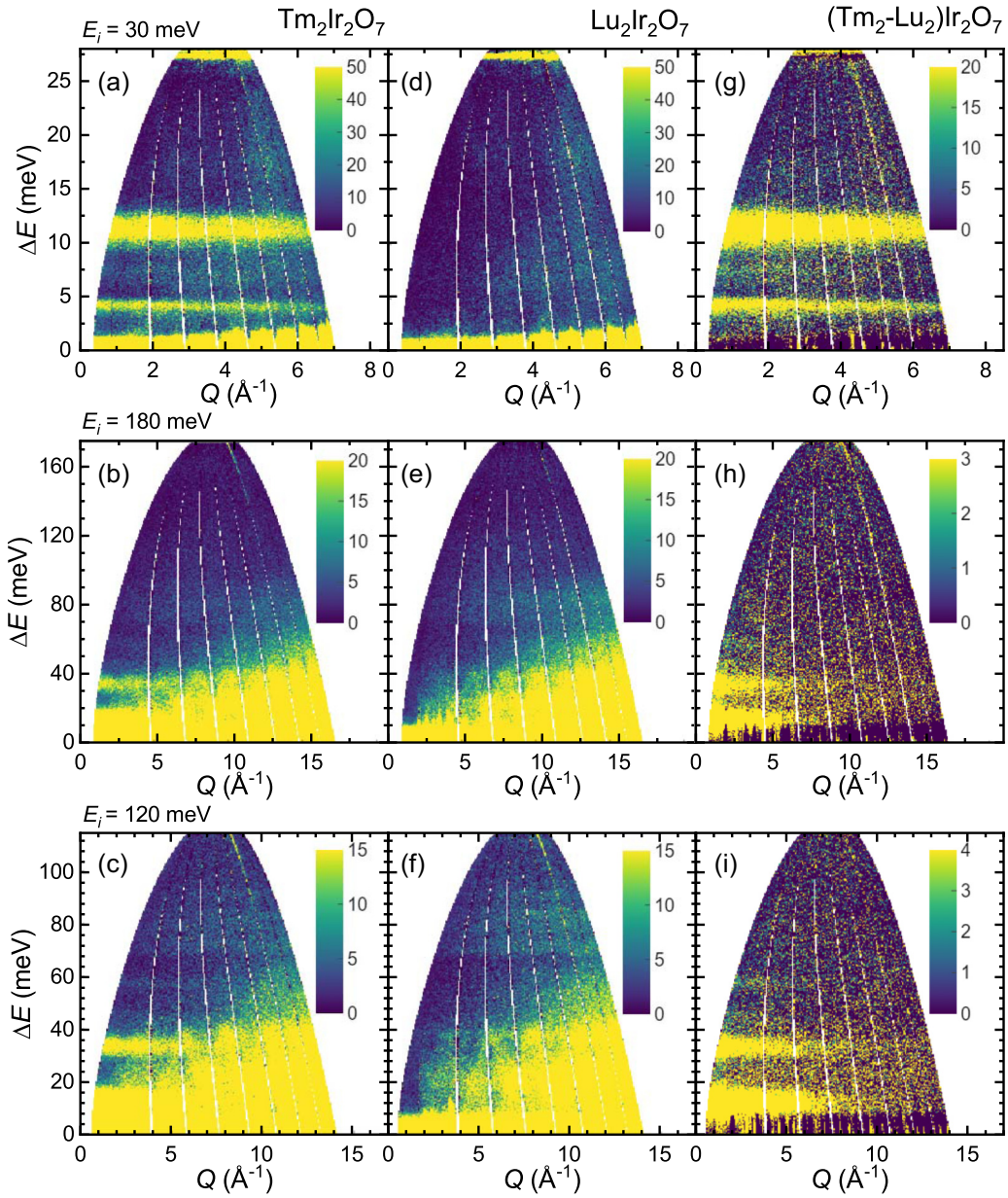

FIG. 3. Inelastic neutron scattering ΔE-Q maps for $Tm_2Ir_2O_7$, $Lu_2Ir_2O_7$, and their difference. The spectra were collected employing incident neutron energies of 30, 180, and 120 meV at 5 K.

symmetries of the two Wyckoff positions are C_{3i} and C_2, respectively. Therefore, Tm_2O_3 reveals two sets of CF excitations, one for each Wyckoff position. The CF scheme connected with a 24*d* position was investigated in detail in the case of Tm-doped nonmagnetic Y_2O_3 [44]. The first observed excitation in our spectra, the pronounced excitation at approximately 3.8 meV, is identified to be the first CF excitation of the 24*d* site scheme. Excitations connected with the 8*b* position were studied only indirectly, investigating a magnetic part of the specific-heat data [45]. According to the specific-heat analysis, the energy of the first CF excitation is 0.5 meV. This excitation cannot be identified in measured INS spectra due to the resolution of the spectrometer (the vicinity of excitation to the elastic peak). The second CF excitation related to the 8*b* site is expected to occur at 7.8 meV [45]. In fact, we observe this excitation in the measured data. The unreacted thulium oxide being responsible for the first two observed magnetic peaks, at 3.8 and 7.8 meV, is supported also by the analysis of magnetic specific-heat data (see Sec. VI). Trials to fit the magnetic excitations of Tm_2O_3 in the measured spectra failed, mainly due to a large number of CF parameters and only a few related (sufficiently intensive) peaks in the spectra. Nevertheless, we calculated the spectrum related to the 24*d* site from known CF parameters [44]. The calculation showed that the intensity of excitations significantly decreases, coming from low to high energies. Indeed, while excitations at 3.8 and 11.0 meV have significant intensity, excitations at 27.2, 28.5, 42.2, 47.4, 54.0, and 60.5 meV (and higher energies) are hardly observable in measured data. See Fig. 4 for details. A reliable estimation of the 8*b* site contribution

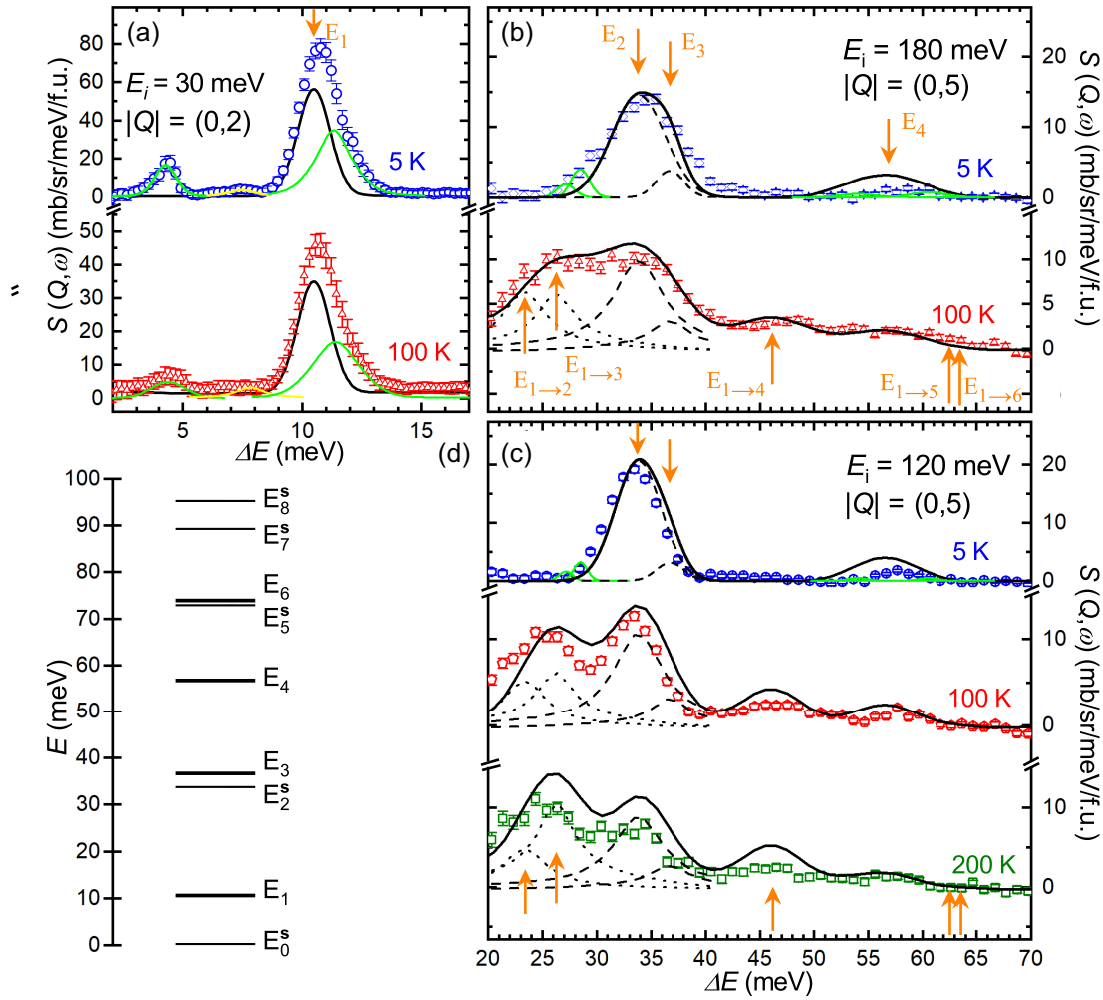

FIG. 4. Low-Q cuts of the difference (magnetic) $Tm_2Ir_2O_7$ spectra. Black lines are the fits (pseudo-Voigt functions) to the $Tm_2Ir_2O_7$ spectra with the CF parameters reported in Table I. Arrows mark the eigenenergies listed in Table I and depicted in panel (d), as well as the energies of excitations between thermally populated levels. The excitations related to the impurity Tm_2O_3 phase are fitted as well: green line for the thulium 24*d* Wyckoff site [44] and yellow line for a single peak identified for the 8*b* site [45]. See text for details.

to spectra cannot be done. Although the sample contains a non-negligible amount of impurity phase (approximately 12%), the following analysis of the crystal-field scheme of $Tm_2Ir_2O_7$ is still valid as the impurity phase contributions are accounted for.

The free Tm^{3+} ion with total angular momentum $J = 6$ has a ground state of $2J + 1 = 13$ times degenerate. In D_{3d} $(-3m)$ point symmetry of Wyckoff position 16*d*: (1/2, 1/2, 1/2)—of the rare-earth atoms in the pyrochlore lattice—the ground-state multiplet of the thulium ion (non-Kramers' ion) is supposed to split into four doublets and five singlets. Therefore, eight excitations from the ground state to the higher-energy states are expected in $Tm_2Ir_2O_7$. Unfortunately, only four excitations were identified in 5 K spectra: excitations at 10.5, 33.8, 36.7, and 56.6 meV. We note that the excitations at 33.8 and 36.7 meV form a single broad peak. Its shape, nevertheless, suggests that it comprises two peaks, as was confirmed by fitting to models described below (see the fits of the two peaks in Fig. 4). Determining the CF scheme of $Tm_2Ir_2O_7$, that is, refinement of six CF parameters, utilizing only four excitations, would, of course, lead to dubious results. Therefore, the following two factors were used:

(i) The model CF schemes of $Tm_2Ir_2O_7$ were calculated by rescaling the CF parameters obtained by the previous INS studies on the $Er_2Ir_2O_7$ [25] and $Yb_2Ir_2O_7$ analogs [23], with Er and Yb having one lower and one higher atomic number than Tm, respectively. Model CF parameters were calculated by scaling the corresponding Stevens factors as described in Sec. III and our recent publication [20]. $Yb_2Ir_2O_7$-based model CF parameters led to a different scheme, noticeably different degeneracy of the individual energy levels (Table I), compared to the $Er_2Ir_2O_7$-based CF scheme. The $Yb_2Ir_2O_7$-based scheme allowed for a significantly worse description of bulk magnetization and specific-heat data, as illustrated in [20]. The spectra calculated from rescaled CF parameters suggest three excitations below and one excitation close to 60 meV, which is well in agreement with the experiment. Inspecting the higher-energy region in the ΔE-Q maps (Fig. 3), no clearly defined magnetic signal is found. Indeed, the calculated intensities of high-energy excitations are order(s) of magnitude lower than those at lower energy. The model CF

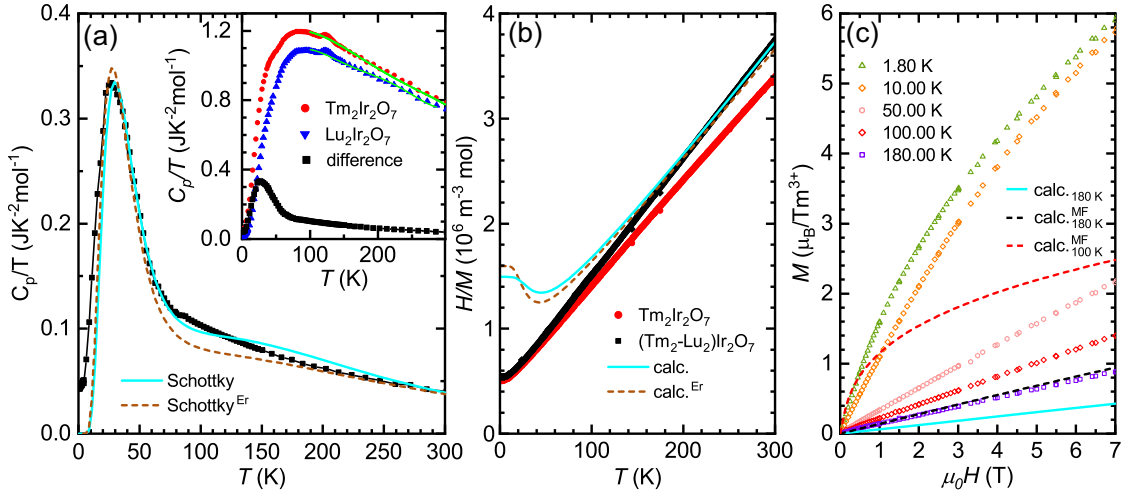

FIG. 5. Specific heat and magnetization of $Tm_2Ir_2O_7$. (a) Magnetic contribution to the specific heat and Schottky contribution calculated from CF eigenenergies. The inset contains the total specific heat of $Tm_2Ir_2O_7$ and $Lu_2Ir_2O_7$ and their difference. (b) Inverse magnetic susceptibility of $Tm_2Ir_2O_7$, difference susceptibility, subtracting $Lu_2Ir_2O_7$ data from $Tm_2Ir_2O_7$ data, and susceptibility calculated from CF parameters (refined CF parameters and Er-analog rescaled parameters, respectively). (c) Isothermal magnetization of $Tm_2Ir_2O_7$ and magnetization curves calculated using a microscopic Hamiltonian with the CF (full blue line for 180 K data) and molecular field term (dashed lines for 180 and 100 K data).

parameters were used as starting values for a refinement of the measured data.

(ii) Data measured with incident energies of 30, 120, and 180 meV at 5, 100, and 200 K were fitted simultaneously. The thermal population of the first excitation level at 10.5 meV (thermal energy $E = k_BT$, where k_B is the Boltzmann constant) at temperatures 100 and 200 K enables transitions from this level to higher CF levels, resulting in new excitations at 23.3, 26.2, 46.1 meV, and a very weak magnetic signal at around 62.3 meV (Fig. 4). Simultaneously, the respective signal appears in the neutron-energy-gain part of the spectra (negative ΔE). Of course, also other excitations/deexcitations between partially thermally populated higher-energy levels are allowed, but they are calculated to have significantly lower intensity. Fitting a larger number of peaks in the spectra allows for a more reliable determination of the crystal-field parameters.

The magnetic (difference) spectra of $Tm_2Ir_2O_7$ were fitted to the model crystal-field Hamiltonian for the (local) point symmetry D_{3d}:

$$\boldsymbol{H}_{\mathbf{CF}} = B_2^0\mathbf{O}_2^0 + B_4^0\mathbf{O}_4^0 + B_4^3\mathbf{O}_4^3 + B_6^0\mathbf{O}_6^0 + B_6^3\mathbf{O}_6^3 + B_6^6\mathbf{O}_6^6, \quad (2)$$

with B_n^m and $\mathbf{O}_n^m$ representing the crystal-field parameters and Stevens operators of the thulium $4f$ shell, respectively. The resulting fits are plotted in Fig. 4, and the corresponding crystal-field parameters and eigenenergies are listed in Table I. We note that identical final CF parameters were refined using both $Er_2Ir_2O_7$-based and $Yb_2Ir_2O_7$-based models of starting CF parameters.

VI. MAGNETIZATION AND SPECIFIC HEAT IN VIEW OF THE DETERMINED CF SCHEME, DISCUSSION

Magnetization and specific heat were measured simultaneously on samples used later for the INS experiment and calculated from refined CF parameters and eigenenergies (Table I, see Sec. III). The comparison of data and calculations is shown in Fig. 5. In the following text, we restrict ourselves to a brief description of measured data; the complete analysis of the magnetization and specific heat of $Tm_2Ir_2O_7$ was recently published elsewhere [20].

The specific heat of $Tm_2Ir_2O_7$ is composed of electronic, lattice, and magnetic contributions of Tm and Ir. To estimate the magnetic contribution of only Tm, the $Lu_2Ir_2O_7$ analog data with no magnetic contribution of Lu^{3+} were subtracted from the $Tm_2Ir_2O_7$ data. The difference data are compared with the Schottky specific heat calculated from the determined CF eigenenergies in Fig. 5(a). A reasonable agreement between the data and the calculation based on the rescaled $Er_2Ir_2O_7$-to-$Tm_2Ir_2O_7$ model energies (red dashed line) is observed (as discussed in detail in [20]). Naturally, even better agreement is seen using the eigenenergies determined from the INS spectra of $Tm_2Ir_2O_7$ (solid blue line). Importantly, this agreement strongly supports our interpretation of INS data. That is, the magnetic excitations at 3.8 and 7.8 meV originate from unreacted Tm_2O_3, and they should not be involved in the fitting of the CF parameters of $Tm_2Ir_2O_7$. Otherwise, a significant difference between the calculated Schottky specific heat (considering one or both of these excitations) and measured data is observed.

The magnetic susceptibility related to the Tm magnetic moments was estimated by subtracting the $Lu_2Ir_2O_7$ data from the $Tm_2Ir_2O_7$ data. Susceptibility was calculated simultaneously (see Sec. III) from both the $Er_2Ir_2O_7$-based model and the refined CF parameters (Table I). The inverse susceptibilities are presented in Fig. 5(b). A good agreement between measurement and calculations is observed down to approximately 200 K. Still, a reasonable agreement is seen between 200 and 70 K. However, at lower temperature, the calculated susceptibility deviates significantly from the measured data. Although the Ir-sublattice contribution was estimated (using

$Lu_2Ir_2O_7$ data) and subtracted from $Tm_2Ir_2O_7$ data, the resulting data below T_{Ir} do not correspond to only Tm contribution. The Tm magnetic properties are influenced by the molecular field induced by Ir sublattice ordering.

The disagreement is pronounced also comparing the mean-field calculations and isothermal magnetization data presented in Fig. 5(c). Calculating the isothermal magnetization considering only the CF contribution, the measured data are described only qualitatively; about half of the measured moment is estimated [full blue line in Fig. 5(c)]. Therefore, we constructed the microscopic Hamiltonian containing the crystal-field part and the Zeeman term with the molecular field. The molecular field $H_{mf} = \lambda\langle M\rangle$, for simplicity along the direction of the external magnetic field, was calculated self-consistently. The molecular field constant λ was adjusted to properly describe the magnetization data (average magnetization $\langle M\rangle$) measured at 180 K (dashed black line). However, calculating the magnetization at 100 K (dashed red line) led to significantly higher values than measured. The simple molecular field approach, which well described the magnetization of other $A_2Ir_2O_7$ [20,23,25], fails to describe the $Tm_2Ir_2O_7$ data.

In our opinion, the simple Heisenberg spin pairwise Hamiltonian also cannot be used to properly regard the complex magnetism of the system. The magnetism of the Ir sublattice, including the orbital contributions induced by the strong SO coupling at the itinerant iridium sublattice, is essential to consider for a proper description of the experimental data.

The refined CF parameters were also compared with the parameters of other $A_2Ir_2O_7$ pyrochlore iridates [8,9,23,25]. We highlight a noticeable systematics within the series. The CF parameters divided by Stevens factors α, β, γ are presented for heavy rare-earth $A_2Ir_2O_7$ pyrochlores in Table II. Values of the same signs and similar magnitudes were determined for all members. On the other hand, the values do not follow, for instance, the contraction of the $4f$ radial wave function [46]. In our opinion, this fact reflects the small changes of hybridization between the rare-earth $4f$ wave function and $2p$-states of eight nearest-neighbor oxygen atoms in the pyrochlore lattice. Such hybridization creates an important contribution to the crystal field in oxides [47].

Strikingly similar systematics is observed for $A_2Ti_2O_7$ counterparts [48]. We emphasize the CF scheme of $Tm_2Ti_2O_7$ with the first CF excitation at 10 meV [49]. No other excitation was observed by inspecting the INS data. However, by scaling the CF parameters of other titanates [48], excitations of (very) low intensity were predicted at 20, 27, 51, 61, 63, 90, and 92 meV. We note the exact same schemes of levels in $Tm_2Ti_2O_7$ and $Tm_2Ir_2O_7$. That is, the ground-state singlet in $Tm_2Ti_2O_7$ is followed by doublets and singlets separated in energy in a very similar way as refined for $Tm_2Ir_2O_7$ (Table I). The same excitation scheme, similar excitation energies, as well as good agreement in comparing the CF schemes of other titanates and iridates [20,23,25,26,48] strongly support our refinement of the INS data and the final set of CF parameters.

Finally, let us briefly discuss the ground-state singlet of Tm^{3+} in $Tm_2Ir_2O_7$, well separated from the first CF doublet. The strength of the crystal-field and exchange interactions effects in the material can be comparable in rare-earth materials under certain circumstances, determining the qualitative nature of magnetic ordering [50]. Specifically, the ground-state singlet state well separated from the first excited state results in no magnetic ordering of the Tm sublattice down to low temperature (at least down to 0.4 K based on measured magnetization and specific-heat data) in $Tm_2Ir_2O_7$. Weak exchange interaction between thulium cations compared to the gap between singlet ground state and first excited state was reported also for the titanium counterpart: $Tm_2Ti_2O_7$ pyrochlore [49], as well as other Tm-based compounds [51,52]. The crystal-field splitting is strong enough to preclude magnetic order also in other non-Kramers ion systems, most notably Pr-based systems [53–58]. However, recent neutron diffraction study on $Tm_2Mn_2O_7$ [59] revealed a magnetic signal that is not consistent with the magnetic moment only on Mn^{4+}. The data were interpreted considering either a lowering of cubic symmetry of the lattice or the Mn-molecular-field induced magnetic moment on Tm. Similarly, the molecular field of Ir sublattice might induce a weak magnetic signal observed in low-temperature powder neutron diffraction patterns (Fig. 2). Indeed, the magnetic signal was observed at low temperature (significantly below T_{Ir}) only. Nevertheless, this speculation, whether the magnetic signal originates in Ir or Tm moments, cannot be unambiguously verified on the basis of measured data. No lowering of the cubic symmetry was observed inspecting diffraction data down to low temperature.

VII. CONCLUSIONS

A $Tm_2Ir_2O_7$ powder sample was synthesized from a stoichiometric mixture of Tm_2O_3 and IrO_2 oxides using the CsCl flux method. The iridate was confirmed to crystallize in a pyrochlore-type of cubic structure. The determined lattice parameter $a^{Tm2Ir2O7} = 10.135(1)$ Å and the fraction coordinate of the Wyckoff oxygen $48f$ position $x^{Tm2Ir2O7}_{O-48f} = 0.335(2)$ agree well with previous studies on $Tm_2Ir_2O_7$ and other members of the series. The pyrochlore crystal structure is preserved down to 0.2 K; no structural change was observed in neutron diffraction patterns. Thermal expansion of the lattice is well described within a Debye model of lattice vibrations. A weak magnetic signal, consistent with the AIAO order, was observed in diffraction patterns. However, no further magnetic peak was tracked; AIAO structure cannot be unambiguously confirmed in $Tm_2Ir_2O_7$ based on measured diffraction data. The crystal-field parameters and the CF eigenenergies were determined by analyzing the inelastic neutron scattering spectra of $Tm_2Ir_2O_7$. Nondispersive magnetic excitations were described by a standard crystal-field model. The determined crystal-field scheme was discussed with respect to the magnetization and specific-heat data under constraints of the mean-field approximation.

ACKNOWLEDGMENTS

This work was supported by the Czech Science Foundation under Grant No. 18-09375Y. The preparation, characterization, and measurement of bulk physical properties on $A_2Ir_2O_7$ samples were performed in MGML [60], which was supported

within the program of Czech Research Infrastructures (Project No. LM2018096). The authors thank CSIC-Ministerio de Ciencia e Innovación of Spain and CRG-D1B for providing beamtime at the Institute Laue-Langevin. The Technical staff of SANE@ILL, Baurand, Bourgeat-Lami, and Joyet are acknowledge for technical support at sub-Kelvin temperatures. The authors gratefully acknowledge the Science and Technology Facilities Council for access to neutron beamtime on the MARI spectrometer at the ISIS facility. We thank also to Dr. Duc Le from ISIS for instrumental and software support.

[1] J. S. Gardner, M. J. P. Gingras, and J. E. Greedan, Rev. Mod. Phys. **82**, 53 (2010).
[2] H. J. Silverstein, K. Fritsch, F. Flicker, A. M. Hallas, J. S. Gardner, Y. Qiu, G. Ehlers, A. T. Savici, Z. Yamani, K. A. Ross, B. D. Gaulin, M. J. P. Gingras, J. A. M. Paddison, K. Foyevtsova, R. Valenti, F. Hawthorne, C. R. Wiebe, and H. D. Zhou, Phys. Rev. B **89**, 054433 (2014).
[3] S. Petit, P. Bonville, I. Mirebeau, H. Mutka, and J. Robert, Phys. Rev. B **85**, 054428 (2012).
[4] B. Tomasello, C. Castelnovo, R. Moessner, and J. Quintanilla, Phys. Rev. B **92**, 155120 (2015).
[5] Y. Tokiwa, J. J. Ishikawa, and S. Nakatsuji, Nat. Mater. **13**, 356 (2014).
[6] J.-J. Wen, S. M. Koohpayeh, K. A. Ross, B. A. Trump, T. M. McQueen, K. Kimura, S. Nakatsuji, Y. Qiu, D. M. Pajerowski, J. R. D. Copley, and C. L. Broholm, Phys. Rev. Lett. **118**, 107206 (2017).
[7] G.-W. Chern, R. Moessner, and O. Tchernyshyov, Phys. Rev. B **78**, 144418 (2008).
[8] V. Cathelin, E. Lefrançois, J. Robert, P. C. Guruciaga, C. Paulsen, D. Prabhakaran, P. Lejay, F. Damay, J. Ollivier, B. Fåk, L. C. Chapon, R. Ballou, V. Simonet, P. C. W. Holdsworth, and E. Lhotel, Phys. Rev. Research **2**, 032073(R) (2020).
[9] E. Lefrancois, V. Cathelin, E. Lhotel, J. Robert, P. Lejay, C. V. Colin, B. Canals, F. Damay, J. Olivier, B. Fak, L. C. Chapon, R. Ballou, and V. Simonet, Nat. Commun. **8**, 209 (2017).
[10] H. Guo, C. Ritter, and A. C. Komarek, Phys. Rev. B **96**, 144415 (2017).
[11] Y. Wang, H. Weng, L. Fu, and X. Dai, Phys. Rev. Lett. **119**, 187203 (2017).
[12] G. Chen and M. Hermele, Phys. Rev. B **86**, 235129 (2012).
[13] E. Lefrancois, V. Simonet, R. Ballou, E. Lhotel, A. Hadj-Azzem, S. Kodjikian, P. Lejay, P. Manuel, D. Khalyavin, and L. C. Chapon, Phys. Rev. Lett. **114**, 247202 (2015).
[14] K. Matsuhira, M. Tokunaga, M. Wakeshima, Y. Hinatsu, and S. Takagi, J. Phys. Soc. Jpn. **82**, 023706 (2013).
[15] W. Witczak-Krempa, G. Chen, Y. B. Kim, and L. Balents, Annu. Rev. Condens. Matter Phys. **5**, 57 (2014).
[16] A. B. Sushov, J. B. Hofmann, G. S. Jenkins, J. Ishikawa, S. Nakatsuji, S. Das Sarma, and H. D. Drew, Phys. Rev. B **92**, 241108(R) (2015).
[17] D. A. Pesin and L. Balents, Nat. Phys. **6**, 376 (2010).
[18] X. Wan, A. M. Turner, A. Vishwanath, and S. Y. Savrasov, Phys. Rev. B **83**, 205101 (2011).
[19] K. Matsuhira, Y. Hinatsu, and S. Takagi, J. Phys. Soc. Jpn. **80**, 094701 (2011).
[20] M. Klicpera, K. Vlášková, and M. Diviš, J. Phys. Chem. C **124**, 20367 (2020).
[21] H. Guo, C. Ritter, and A. C. Komarek, Phys. Rev. B **94**, 161102(R) (2016).
[22] S. M. Disseler, Ch. Dhital, A. Amato, S. R. Giblin, C. de la Cruz, S. D. Wilson, and M. J. Graf, Phys. Rev. B **86**, 014428 (2012).
[23] H. Jacobsen, C. D. Dashwood, E. Lhotel, D. Khalyavin, P. Manuel, R. Stewart, D. Prabhakaran, D. F. McMorrow, and A. T. Boothroyd, Phys. Rev. B **101**, 104404 (2020).
[24] R. Asih, A. Noraina, S. S. Mohd-Tajudin, K. Matsuhira, H. Guo, M. Wakeshima, Y. Hinatsu, T. Nakano, Y. Nozue, S. Sulaiman, M. I. Mohamed-Ibrahim, P. K. Biswas, and I. Watanabe, J. Phys. Soc. Jpn. **86**, 024705 (2017).
[25] K. Vlášková, P. Proschek, M. Diviš, D. Le, R. H. Colman, and M. Klicpera, Phys. Rev. B **102**, 054428 (2020).
[26] K. Vlášková, M. Diviš, and M. Klicpera, J. Magn. Magn. Mater. **538**, 168220 (2021).
[27] K. Vlášková, R. H. Colman, and M. Klicpera, Mater. Chem. Phys. **258**, 123868 (2021).
[28] D. F. Abbott, R. K. Pittkowski, K. Macounová, R. Nebel, E. Marelli, E. Fabbri, I. E. Castelli, P. Krtil, and T. J. Schmidt, ACS Appl. Mater. Interfaces **11**, 37748 (2019).
[29] K. Vlášková, P. Proschek, J. Pospíšil, and M. Klicpera, J. Crystal Growth **546**, 125783 (2020).
[30] J. Rodrìguez-Carvajal, Physica B **192**, 55 (1993).
[31] M. Klicpera, M. Boehm, P. Doležal, H. Mutka, M. M. Koza, S. Rols, D. T. Adroja, I. Puente Orench, J. Rodríguez-Carvajal, P. Javorský, Phys. Rev. B **95**, 085107 (2017).
[32] M. Klicpera, D. T. Adroja, K. Vlášková, M. Boehm, H. Mutka, B. Ouladdiaf, T. Guidi, and P. Javorký, Inorganic Chemistry **56**, 12839 (2017).
[33] I. Puente Orench and M. Klicpera, *Magnetic Ordering in Newly-synthesised Tm2Ir2O7 Pyrochlore Oxide* (Institut Laue-Langevin, Grenoble, France, 2021).
[34] J. Taylor, O. Arnold, J. Bilheaux, A. Buts, S. Campbell, M. Doucet, N. Draper, and R. Fowler, Bull. Am. Phys. Soc. **57**, W26.00010 (2012).
[35] M. Klicpera, K. Vlášková, D. Le, and T. Guidi, Magnetic excitations in newly synthesized $Tm_2Ir_2O_7$ pyrochlore iridate (Science and Technology Facilities Council (STFC) ISIS Neutron and Muon Source, 2021), doi: 10.5286/ISIS.E.RB2000237.
[36] K. Vlášková, R. H. Colman, P. Proschek, J. Čapek, and M. Klicpera, Phys. Rev. B **100**, 214405 (2019).
[37] M. Klicpera, K. Vlášková, R. H. Colman, P. Proschek, and A. Hoser, Acta Phys. Pol. A **137**, 750 (2020).
[38] F. Sayetat, P. Fertey, and M. Kessler, J. Appl. Cryst. **31**, 121 (1998).
[39] M. Klicpera, K. Vlášková, and M. Diviš, J. Magn. Magn. Mater. **506**, 166793 (2020).
[40] L. Hozoi, H. Gretarsson, J. P. Clancy, B.-G. Jeon, B. Lee, K. H. Kim, V. Yushankhai, P. Fulde, D. Casa, T. Gog, J. Kim, A. H.

Said, M. H. Upton, Y.-J. Kim, and J. van den Brink, Phys. Rev. B **89**, 115111 (2014).
[41] J. P. Clancy, H. Gretarsson, E. K. H. Lee, D. Tian, J. Kim, M. H. Upton, D. Casa, T. Gog, Z. Islam, B.-G. Jeon *et al.*, Phys. Rev. B **94**, 024408 (2016).
[42] D. Uematsu, H. Sagayama, T. H. Arima, J. J. Ishikawa, S. Nakatsuji, H. Takagi, M. Yoshida, J. Mizuki, and K. Ishii, Phys. Rev. B **92**, 094405 (2015).
[43] The Materials Project, Materials Data on Tm2O3 by Materials Project, USA.
[44] T. Chanelière, J. Ruggiero, J.-L. Le Gouët, W. Tittel, J.-H. Mun, A. Jouini, A. Yoshikawa, G. Boulon, Y. L. Du, Ph. Goldner, F. Beaudoux, J. Vincent, E. Antic-Fidancev, and O. Guillot-Noël, Phys. Rev. B **77**, 245127 (2008).
[45] Ł. Gondek, D. Kaczorowski, and A. Szytuła, Solid State Commun. **150**, 368 (2010).
[46] A. J. Freeman and J. P. Desclaux, J. Magn. Magn. Mater. **12**, 11 (1979).
[47] P. Novák, K. Knížek, and J. Kuneš, Phys. Rev. B **87**, 205139 (2013).
[48] A. Bertin, Y. Chapuis, P. Dalmas de Réotier, and A. Yaouanc, J. Phys.: Condens. Matter **24**, 256003 (2012).
[49] M. P. Zinkin, M. J. Harris, Z. Tun, R. A. Cowley, and B. M. Wanklyn, J. Phys.: Condens. Matter **8**, 193 (1996).
[50] B. R. Cooper and O. Vogt, J. Phys. (Paris) Colloq. C1, suppl. 2-3 **32**, C1-958 (1971).
[51] D. P. Schumacher and W. E. Wallace, J. Appl. Phys. **36**, 984 (1965).
[52] H. Winter, D. Shaltiel, and E. Dormann, J. Magn. Magn. Mater. **87**, 181 (1990).
[53] B. D. Rainford and J. Gylden Houmann, Phys. Rev. Lett. **26**, 223 (1971).
[54] J. Jensen and A. R. Mackintosh, Int. Ser. Monographs Phys. **81**, 361 (1991).
[55] K. Marumoto, F. Takayama, and Y. Mayako, J. Magn. Magn. Mater. **177-181**, 353 (1998).
[56] M. Klicpera, J. Fikáček, K. Vlášková, I. Puente Orench, M. Diviš, and P. Javorský, J. Alloys Comp. **781**, 1189 (2019).
[57] D. T. Adroja and V. K. Anand, Phys. Rev. B **86**, 104404 (2012).
[58] M. Klicpera, J. Pastzorová, and P. Javorský, Supercond. Sci. Technol. **27**, 85001 (2014).
[59] E. Pomjakushina, V. Pomjakushin, K. Rolfs, J. Karpinski, and K. Conder, Inorg. Chem. **54**, 9092 (2015).
[60] http://mgml.eu/.